

PAPER • OPEN ACCESS

Self-assembled PCBM bilayers on graphene and HOPG examined by AFM and STM

To cite this article: Yanlong Li *et al* 2018 *Nanotechnology* **29** 185703

View the [article online](#) for updates and enhancements.

Self-assembled PCBM bilayers on graphene and HOPG examined by AFM and STM

Yanlong Li¹, Chuanhui Chen^{1,2}, John Burton¹, Kyungwha Park¹,
James R Heflin¹ and Chenggang Tao^{1,2,3} 

¹Department of Physics, Virginia Tech, Blacksburg, VA 24061, United States of America

²Center for Soft Matter and Biological Physics, Virginia Tech, Blacksburg, VA 24061, United States of America

E-mail: cgtao@vt.edu

Received 19 July 2017, revised 10 February 2018

Accepted for publication 16 February 2018

Published 8 March 2018



CrossMark

Abstract

In this work we report fabrication and characterization of phenyl-C61-butyric acid methyl ester (PCBM) bilayer structures on graphene and highly oriented pyrolytic graphite (HOPG). Through careful control of the PCBM solution concentration (from 0.1 to 2 mg ml⁻¹) and the deposition conditions, we demonstrate that PCBM molecules self-assemble into bilayer structures on graphene and HOPG substrates. Interestingly, the PCBM bilayers are formed with two distinct heights on HOPG, but only one unique representative height on graphene. At elevated annealing temperatures, edge diffusion allows neighboring vacancies to merge into a more ordered structure. This is, to the best of our knowledge, the first experimental realization of PCBM bilayer structures on graphene. This work could provide valuable insight into fabrication of new hybrid, ordered structures for applications to organic solar cells.

Keywords: graphene, atomic force microscopy, scanning tunneling microscopy, PCBM, self-assembly

(Some figures may appear in colour only in the online journal)

1. Introduction

In the past several decades, organic solar cells have attracted tremendous scientific and industrial interest because their power conversion efficiency has dramatically increased and reached about 14% to date [1–3]. In addition, organic solar cells have potential advantages compared to traditional solar cells in flexibility of chemical modification as well as low-cost mass production [4]. Typically, an organic solar cell generates electric current through photon-induced electron transfer that separates electrons from holes [5]. Function of a solar cell depends on materials serving as electron donor and electron acceptor, respectively. As light enters a solar cell, the

photons induce the electrons to transfer from the excited state of the donor to the lowest unoccupied molecular orbital of the acceptor. Subsequently, the separated electrons and holes reach the cathode and anode, respectively, delivering a direct current to an outer circuit [6]. The power conversion efficiency of a solar cell depends on various properties including electron affinity of electron acceptor.

The overall performance of organic solar cells hinges on material properties of an active layer, which is composed of a variety of donors (e.g., poly[2-methoxy-5-(3',7'-dimethyloctyloxy)-1,4-phenylenevinylene] (MDMO-PPV), poly(3-hexylthiophene-2,5-diyl) (P3HT) [7–10]) and acceptors (e.g., phenyl-C61-butyric acid methyl ester (PCBM) [11, 12]). There have been intensive previous investigations on the various factors that impact the efficiency of organic solar cell devices, such as solvent/thermal annealing, weight ratio of donor and acceptor, thickness of the active layer, etc [13–16]. In the past several years, utilization of emerging two-dimensional (2D) materials such as graphene for energy-related applications have attracted major research efforts [17–19]. Notably, graphene is a promising

³ Author to whom any correspondence should be addressed.

candidate for a transparent electrode material in solar cells [20–23]. To design efficient organic/2D material hybrid solar cells, it is crucial to understand the morphology of the donor/acceptor nanostructures on 2D materials. Although morphology of donor/acceptor nanostructures has been well characterized on bulk substrates, such as metals or ITO [14, 24–36], similar studies on 2D materials are still lacking.

In this work, we present the self-assembled structure of PCBM, a promising acceptor material for organic solar cells, deposited on graphene and HOPG. We discover novel bilayer nanostructures of PCBM on graphene and HOPG, and investigated how thermal annealing tunes the morphology of the PCBM bilayer, by using AFM and STM. Interestingly, PCBM bilayers are formed with two typical heights on HOPG, but only one on graphene. At different annealing temperatures, edge diffusion causes neighboring vacancies to emerge into a more ordered structure. This first experimental realization of PCBM bilayer structures on graphene may pave a way to fabricate hybrid structures of organic donor/acceptor molecules and graphene for applications in organic solar cells.

2. Experimental methods

PCBM was purchased from NanoC Inc. (Purity: 99.5%). A solution of PCBM was prepared by stirring PCBM powder in chlorobenzene and then the solution was set on a hot plate at about 70 °C for 24 h. The film samples were prepared by spin-coating the solution onto freshly cleaved HOPG substrate (SPI-1 grade, purchased from SPI supplies) or graphene on Cu foils synthesized by CVD. AFM measurements were carried out on a Dimension Icon (Bruker Corporation) instrument in a dark environment. Monolithic silicon cantilevers (NCST, NANO WORLD) with a spring constant of 7.4 N m^{-1} , first longitudinal resonance frequencies between 120 and 205 kHz, and nominal tip radius of 8 nm were employed in soft tapping mode. Simultaneous height and phase images were acquired and reproduced across multiple samples. STM characterizations were carried out in an ultra-high vacuum scanning tunneling microscope system (Omicron STM) with a base pressure of low 10^{-9} Torr. The STM tip was a chemically etched tungsten tip.

3. Results and discussion

3.1. PCBM bilayer morphology

We first investigated the self-assembled structure of PCBM deposited on a graphene/Cu substrate. The main facet of Cu underneath monolayer graphene is (111) oriented, which was determined by typical Moiré patterns of graphene (inset of figure 1(a)). Typical AFM topography images of the PCBM bilayer on graphene (figures 1(b)–(d)), showed a random distribution of PCBM islands, similar to previous SEM results [37], in contrast to highly ordered hcp or ‘double row’ structures such as have been previously reported [38, 39].

These islands are identified as PCBM bilayers with a measured height of $\sim 1.37 \text{ nm}$ (figures 1(d) and (e), blue lines), which is close to double the diameter of PCBM molecules ($\sim 0.7 \text{ nm}$). The height of this domain differs significantly from the height of chlorobenzene residue and a height of PCBM monolayer [38], and so we can exclude the possibility that the connected islands are due to solvent or PCBM monolayers.

In order to characterize the large-scale morphology of such a PCBM domain, we also deposited PCBM bilayer nanostructures on a HOPG substrate, which provides much larger atomically flat terraces in comparison with the flat facets in the case of the graphene/Cu substrate. The lowest coverage (~ 0.15) bilayer films on HOPG were spin-coated from 0.1 mg ml^{-1} PCBM in chlorobenzene solution (figure 1(h)). Atomically resolved STM images of the area outside the film domain verified that it was bare HOPG substrate (insert of figure 1(h)). The PCBM bilayer film showed continuity when crossing step edges on the HOPG substrate (figure 1(h), white double arrows). The overall differences between figures 1(b) (long stripes) and 1(f), (h), and (i) (irregular islands) are due to the differences between the underlying graphene/Cu and HOPG substrates. Spin-coating from higher concentrations of PCBM resulted in higher coverage of the substrate by PCBM bilayers, but the morphology of the bilayer remained as irregular networks with randomly distributed holes. Figure 1(k) is a plot of the coverage of PCBM on HOPG versus the concentration of the PCBM/Chlorobenzene solution.

Strikingly, we found two typical heights in the PCBM bilayer deposited on the HOPG substrate: $1.64 \pm 0.09 \text{ nm}$ (Type I, blue line in figure 1(f)), and $1.23 \pm 0.03 \text{ nm}$ (Type II, red lines in figures 1(f) and (i)). In some films, one type of PCBM bilayer dominated the sample (figure 1(i)), while in others the two types coexisted in a sample (figure 1(f)). Our observations of PCBM monolayers, which will be discussed in the following section, showed a very different height, and hence we exclude the possibility that the Type II structure originates from a monolayer. Combining the above observations together, we conjecture that the height difference reflects two distinct types of the PCBM dimer-HOPG substrate interaction with different arrangement angles leading to different heights.

Note that these novel PCBM bilayers were observed on graphene and HOPG surfaces rather than monolayers with hexagonal close-packed structures [28, 38] or double row structures on Au surfaces [38, 39]. The typical height of a PCBM monolayer is about 0.7 nm, and the height of a PCBM bilayer is 1.64 nm. It is most likely that the observed PCBM bilayer structure consists of PCBM dimers standing up on the graphene surface with some tilt angle due to the weak interaction between PCBM dimers and the graphene surface. The tilt angle between PCBM dimers and the graphene surface is about 40.6° . In a previous theoretical study, Bredas’ group found a similar structure where pentacene molecules on a gold surface are tilted with an angle of about 37.7° [40].

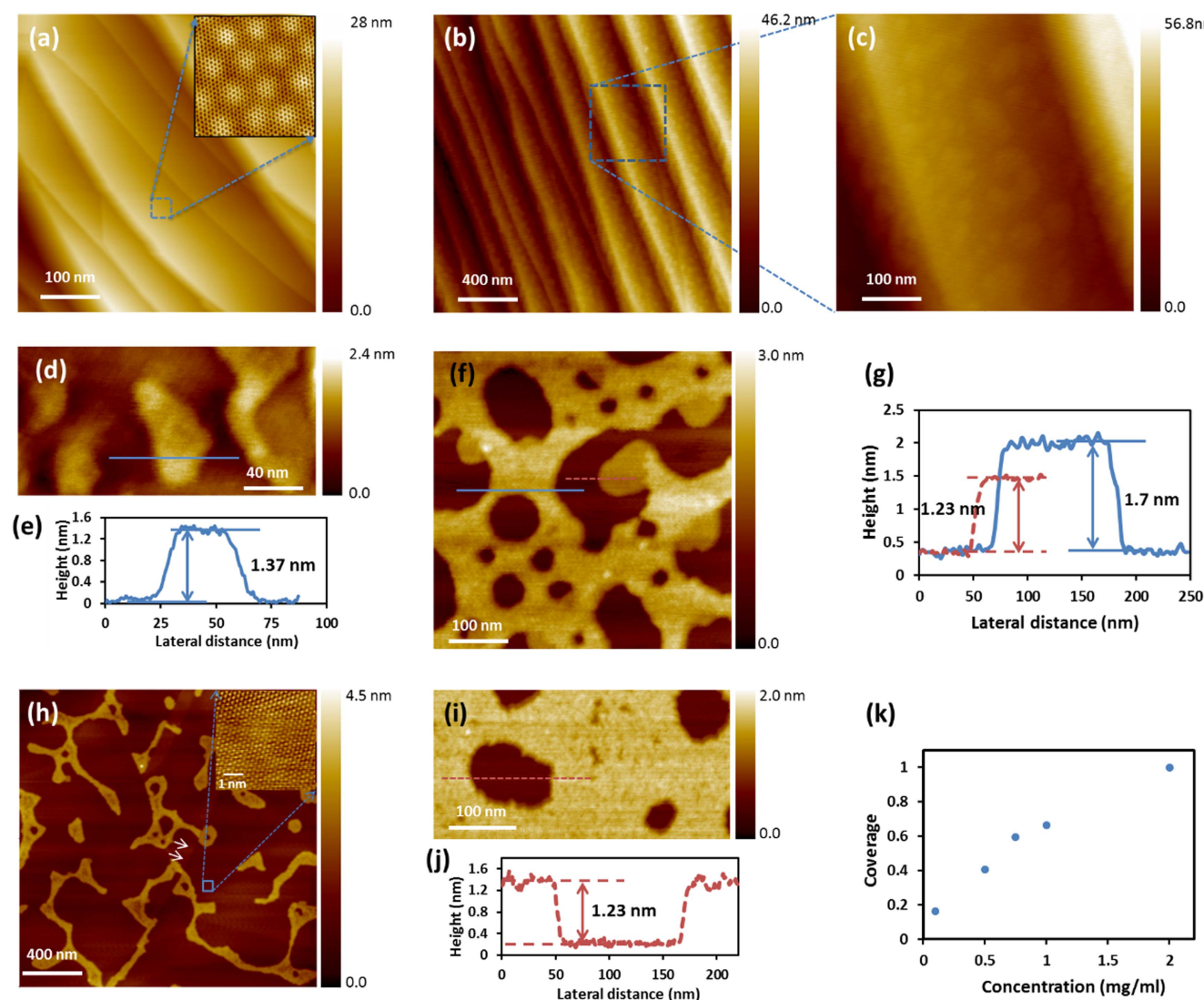


Figure 1. AFM and STM images of PCBM films spin-coated from PCBM/Chlorobenzene solution on graphene/Cu and HOPG substrates. (a) STM image of a graphene/Cu substrate, and the insert is the atomic image of Moiré pattern of graphene on Cu (111) taken from the white square area in figure 1(a). (b) AFM image of a PCBM bilayer on a graphene/Cu substrate from 0.2 mg ml^{-1} PCBM solution. (c) AFM image of a PCBM bilayer on a graphene/Cu substrate from blue square area in figure 2(c). (d) A zoomed in AFM image of a PCBM bilayer on a graphene/Cu substrate (e) line profile with the height about 1.37 nm. (f) AFM image of PCBM bilayer on HOPG substrate from 0.5 mg ml^{-1} PCBM solution. (g) Line profiles with the heights of type I (blue line) and type II (red dashed line) indicated in figure 1(f). (h) AFM image of 0.15 PCBM bilayer on HOPG from 0.1 mg ml^{-1} PCBM solution; the insert is an atomically resolved STM image of bare HOPG substrate taken from the white square area. In figure 1(h), the HOPG step edges are indicated by white double arrows. (i) AFM image of a PCBM bilayer on HOPG substrate from 1.0 mg ml^{-1} solution. (j) Line profile showing the height of type II (red dashed line) showed in figure 1(i). (k) Coverage of PCBM on HOPG versus concentration of the PCBM/Chlorobenzene solution.

3.2. PCBM monolayer morphology

Next, we examine self-assembled PCBM monolayers deposited on graphene/Cu and HOPG. On graphene, a monolayer was formed after a post annealing for 30 min at 170°C (figures 2(a) and (b)). On HOPG, the monolayer sample is more favorable as the stabilization time of the solution increases. The overall morphology resembles the irregular network observed in the bilayer structure (figures 2(a) and (b)). The figure indicates the morphology of a PCBM monolayer on the graphene/Cu substrate, while the inserted line profile shows the height is about 0.87 nm, which is in the range of monolayer height. In order to further examine

monolayers, additional PCBM monolayer samples were studied by spin coating 0.5 mg ml^{-1} PCBM/Chlorobenzene solution on HOPG under the same deposition conditions as the bilayer samples. The height of a monolayer has two typical values on the HOPG substrate: one is around 0.71 nm (figures 2(c) and (d)); the other one is about 0.88 nm (figures 2(e) and (f)). These two values are relatively close to each other, and both of them are comparable to those reported in previous literature [38, 39]. Thus, it is suggested that both of these two heights originate from PCBM monolayers with different orientations. Compared to the mixed structures that can be observed in the bilayers, these two typical heights always appear in different samples, which may be due to a

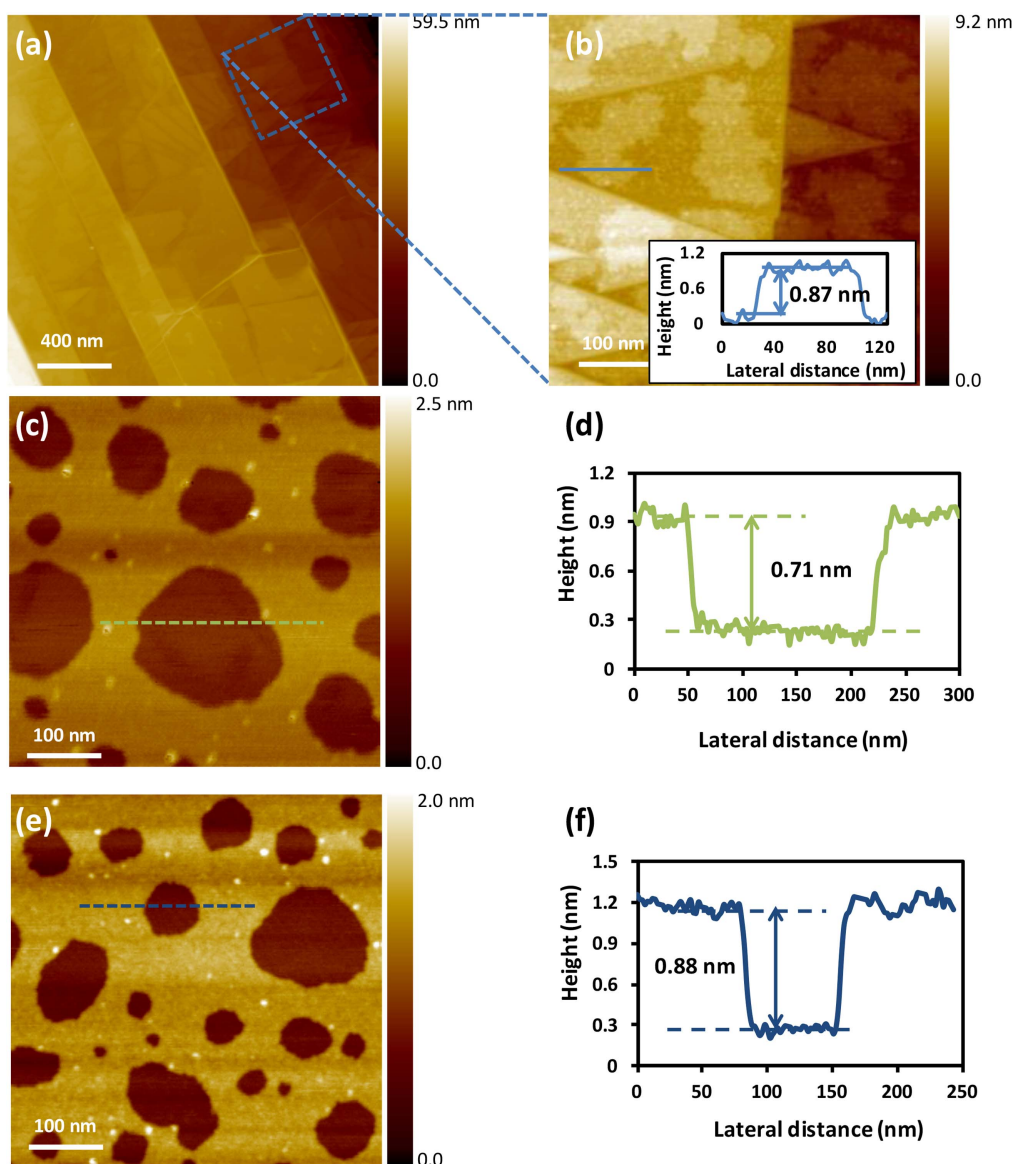


Figure 2. AFM images of PCBM monolayer films spin-coated from PCBM/chlorobenzene solution on graphene/Cu and HOPG substrates. (a) AFM image of a PCBM monolayer on graphene/Cu from 0.5 mg ml^{-1} PCBM solution after a 30 min 170°C anneal. (b) AFM image of a PCBM monolayer on a graphene/Cu substrate from blue square area in figure 2(b), and the insert is the line profile for typical PCBM monolayer with height of 0.87 nm. (c) AFM image of a PCBM monolayer on HOPG from 0.5 mg ml^{-1} PCBM solution. (d) Line profile along the line marked in (c) indicates the height of 0.71 nm. (e) AFM image of a PCBM monolayer on HOPG from 0.5 mg ml^{-1} solution. (f) Line profile along the line marked in (e) shows the height is about 0.88 nm.

higher energy barrier (1 kcal mol^{-1} —about 200°C thermal energy) between the two PCBM monolayer orientations [38]. Note that our PCBM monolayer sample is filled with randomly shaped monolayer terraces, in contrast to elbow nucleating structure found previously [39].

3.3. Discussion

To understand the observed bilayer and monolayer structures, we construct molecular models based on van der Waals interactions between neighboring fullerene moieties, hydrogen-bonding between tail functional groups, and the interactions between molecules and substrates. We first discuss the model for the monolayer structure. We propose that the two typical monolayer heights of ~ 0.9 and ~ 0.7 nm observed in

the PCBM monolayers reflect different orientations of the PCBM relative to the substrate. The thicker monolayer (~ 0.9 nm) corresponds to a vertical configuration of PCBM, with its tail perpendicular to the HOPG surface (figure 3(a)), whereas the thinner monolayer (~ 0.7 nm) corresponds to a horizontal configuration, with PCBM tails parallel to the HOPG surface and interacting in pairs (figure 3(b)). The monolayer height of 0.7 nm is consistent with the previous measurement of the size of C_{60} by Robey's group [38], while the monolayer height of 0.9 nm has never been reported.

Now we turn to the small differences between the modeled and measured heights of a PCBM monolayer in both of the proposed configurations. These differences arise from the fact that the tapping mode AFM tends to underestimate the

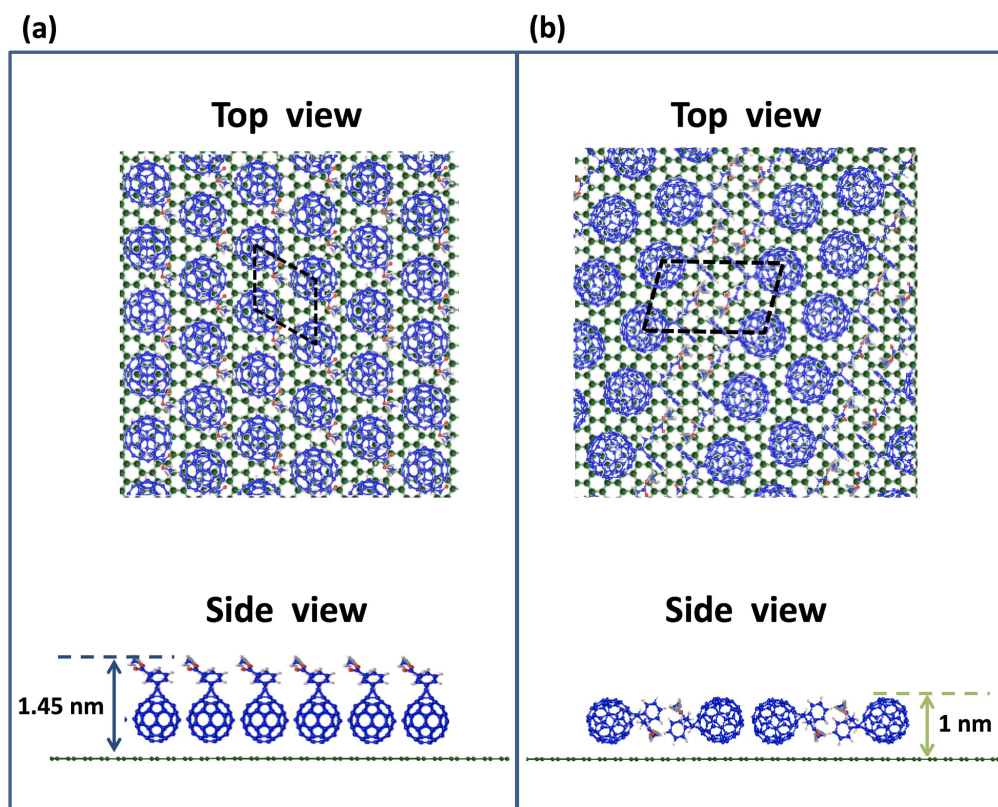


Figure 3. Two schematic model configurations of a PCBM monolayer on a graphene or HOPG substrate: C atom in PCBM (blue), C atom in the substrate (green), O atom (red), and H atom (yellow). (a) Top and side views of one model configuration of a PCBM monolayer with height of 0.9 nm (b) top and side views of another model configuration of a PCBM monolayer sample with height of 0.7 nm. The dashed parallelograms in (a) and (b) indicate unit cells.

height of sample surface features, and that the underestimate amount depends on the stiffness of the measured areas [41, 42]. For the horizontal configuration, the actual monolayer height should be ~ 1 nm, because the equilibrium van der Waals gap between C_{60} and the HOPG substrate is calculated to be 0.25–0.3 nm wide (figure 3) [38]. But due to pressure exerted by the AFM tip, the monolayer height was measured at ~ 0.7 nm. In fact, this measured value is comparable to a previous AFM tapping mode image of a C_{60} shuttlecocks monolayer on HOPG [41]. For the vertical configuration, the monolayer height that the model suggests is 1.45 nm, marking an even larger difference from the measured height of 0.9 nm. This large difference is likely due to softness of the monolayer caused by the PCBM tail groups—these tails are likely much softer than the stiff C_{60} cages in the horizontal configuration.

Our analysis also suggests that a higher coverage of the monolayer favors the vertical configuration. This is reasonable because this configuration can accommodate a much higher area density (1.15 molecule nm^{-2}) of PCBM than that of the horizontal configuration (0.73 molecule nm^{-2}). Using the energy values of neighboring fullerene moieties, the hydrogen-bonding, and the interactions between molecules and substrates from previous experimental and theoretical investigations [38, 39, 43], we calculated the formation energy of these two configurations and the results show an energy barrier of about 1 kcal mol^{-1} exists between the two

configurations, which inhibits thermally-induced transition between the configurations at room temperature.

We now discuss the model for the PCBM bilayer. In most cases, we observed PCBM bilayers rather than monolayers on graphene and HOPG. As described in section 3.1, there are two typical heights in PCBM bilayers on graphene and HOPG: 1.64 nm (modeled in figure 4(a)), and 1.23 nm (modeled in figure 4(b)). It was previously reported that on a gold substrate, PCBM dimers are formed with a twin chain structure in low density, but with a double row structure in high density [38, 39, 44], because the affinity between C_{60} cages (0.28 eV) [44–46] is higher than the hydrogen bonding between the PCBM tail groups (0.114 eV) [44]. However, in this work, PCBM molecules were deposited by spin coating rather than physical vapor deposition. It is known that steric hindrance of sidechain-substituted PCBM molecules would forbid a possibility of a C_{60} -to- C_{60} coordinated structure in the region defined by their first solvation shells [47]. Considering hydrogen bonding and dipole–dipole interactions, the energy of a side-to-side dimer (0.114 eV) is higher than side-to- C_{60} dimer (0.001 eV) [44]. Hence, we suggest that the PCBM molecules form side-to-side dimers in the chlorobenzene solvent before the spin coating. After the spin coating, the side-to-side PCBM dimers are distributed on the HOPG, forming a PCBM bilayers (type I and type II in figure 4). For the thicker bilayer, we propose that the PCBM dimers form a ‘double hcp’ structure: one C_{60} cell of the

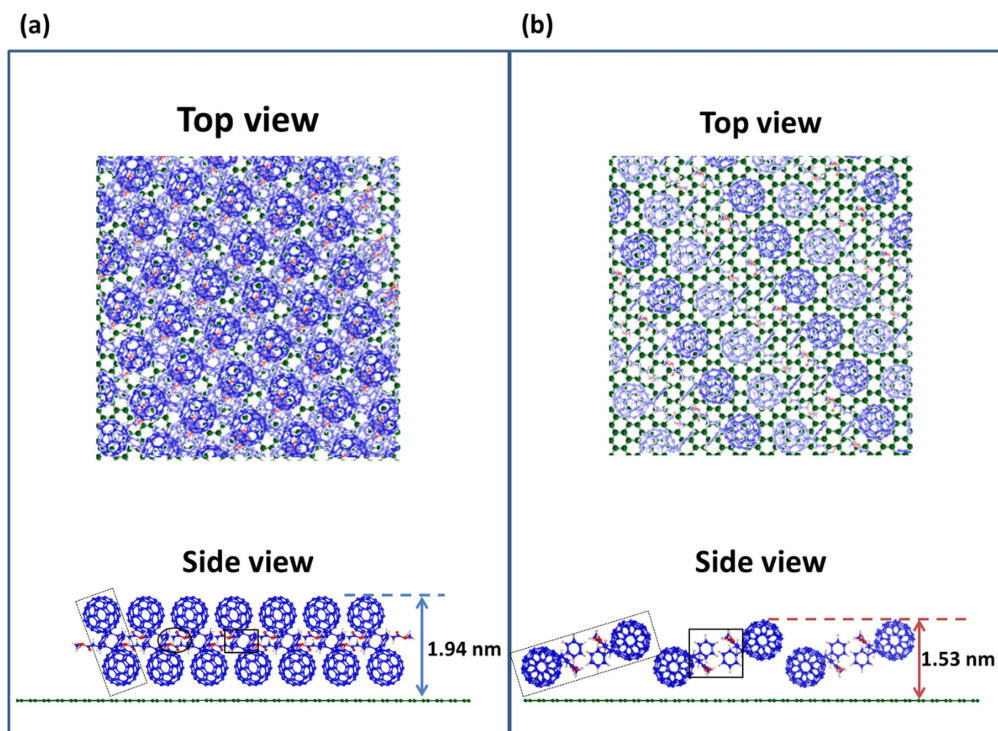


Figure 4. Schematic diagrams of type I and type II configurations of a PCBM bilayer on a graphene or HOPG substrate: C atom in PCBM (blue), C atom in the substrate (green), O atom (red), and H atom (yellow). (a) Top and side views of type I configuration of the PCBM bilayer. In the side view, the dashed tilted rectangle highlights a PCBM dimer cell, and the solid circle indicates the hydrogen binding within a PCBM dimer, while the solid circle shows a side interaction between neighboring PCBM dimers. (b) Top and side views of type II configuration of the PCBM bilayer. In the side view, the dashed tilted rectangle highlights a PCBM dimer cell, while the solid rectangle indicates the hydrogen binding within a PCBM dimer.

dimer lies in the lower layer, the other in the upper layer, such that neighboring PCBM dimers interact sideways (Type I, figure 4(a)). For the thinner bilayer, the PCBM monomers in each dimer are also located in the lower and upper layers (Type II, figure 4(b)), but without strong sideways interactions between PCBM dimers. The two typical PCBM bilayer heights indicates the different tilt angles between a PCBM dimer and the substrate in the two configurations. A tilt angle of 49.4° corresponds to the 1.64 nm bilayer, while a tilt angle of 60.8° the 1.23 nm bilayer, where the tilt angle is defined to be an angle between an axis connecting the centers of two C_{60} in a given dimer and the direction normal to the substrate. Similar to the PCBM monolayer case, the measured heights of a PCBM bilayer are ~ 0.3 nm smaller than those predicted by the model in both configurations. These differences can be similarly explained by the compression caused by the AFM tips.

We further estimate the energy per unit area for the different monolayer and bilayer configurations in order to deduce their relative stability. For Type I bilayer, the binding energy of one upper layer cell of PCBM is 2.52 eV, which arises from the sum of the binding energy of the 9 nearest C_{60} molecules with 0.28 eV each; for the lower layer PCBM cells, the binding energies are 3.5 eV each, which arises from the sum of the binding energy of the 9 nearest C_{60} molecules and of the binding energy between C_{60} and the HOPG (0.98 eV) [43, 48]. Combining the above information with hydrogen binding energies of the neighboring tail groups, we find that

the total energy for each Type I PCBM dimer is 6.13 eV. For Type II bilayer, the upper-layer PCBM cell only has a binding energy of 1.12 eV (4 nearest C_{60}), while the lower-layer PCBM cell on HOPG has a binding energy of 2.1 eV, considering the binding energy of one C_{60} and HOPG and the binding energy of the nearest C_{60} molecules. The binding energy of each PCBM dimer is 3.33 eV. Combining the above information with the hydrogen bonding of the tail groups, we find that for the horizontal configuration the binding energy one PCBM dimer is 4.31 eV. Considering the dimer concentration density of 1.15 dimer nm^{-2} , we find that the energy density of Type I PCBM bilayer is 7.05 eV nm^{-2} , which is higher than that of Type II bilayer by 1.35 eV nm^{-2} and that of the horizontal monolayer by 1.57 eV nm^{-2} . As concentration density increases, the PCBM dimers are compressed to form more vertical configurations in order to accommodate more PCBM dimers on the HOPG surface.

3.4. Thermal effects

We now investigate annealing effects on the morphology of the PCBM bilayer nanostructures. In order to quantify the large-scale morphology changes of PCBM domains, we focused on the PCBM bilayer nanostructures on HOPG substrates, which provide large atomically flat terraces. For this experiment, we annealed the samples at 140 °C and 160 °C for 10 min and measured the samples by AFM immediately after annealing. Figure 5(a) shows the

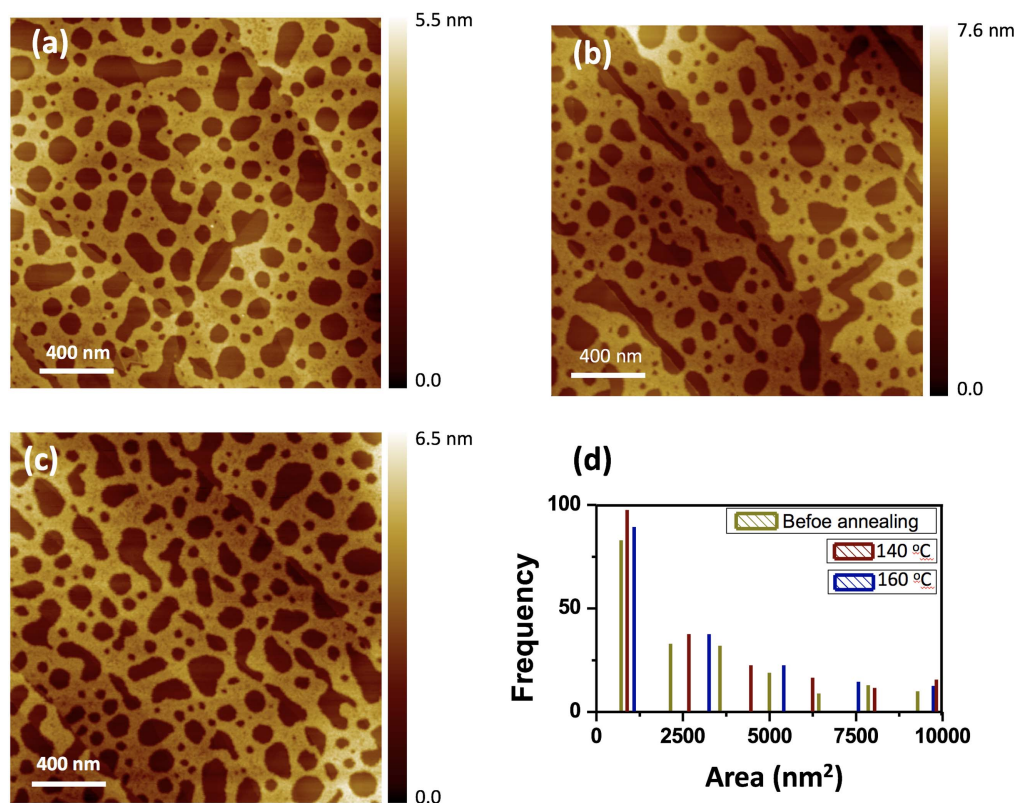


Figure 5. AFM images of PCBM bilayer and size distributions of holes at different conditions. (a) AFM image of a PCBM bilayer before annealing. (b) AFM image of a PCBM bilayer after annealing at 140 °C. (c) AFM image of a PCBM bilayer after annealing at 160 °C. (d) Area distribution histogram of holes (without PCBM area) obtained from measurements of the area of holes in AFM images of before (green) and after annealing at 140 °C (dark red) and 160 °C (dark blue).

topography before annealing and figures 5(b) and (c) are the PCBM bilayer after 140 °C and 160 °C annealing, respectively. To quantify the morphology changes, we performed size distribution analysis for the holes (i.e., bare HOPG area without PCBM) as shown in figure 5(d). by using the standard nanoparticle size distribution analysis method [49]. For data analysis, we use the method introduced in ‘on optimal and data-based histograms’ [50]. We find a right shift of the distribution peak after annealing at 140 °C and 160 °C. The peaks are located at 1490 nm² before annealing, 1884 nm² for annealing at 140 °C, and 2291 nm² for annealing at 160 °C, respectively. The result indicates that the smaller holes are merged together.

4. Summary

In summary, we demonstrated the self-assembly of PCBM bilayer nanostructures on graphene and HOPG, by using AFM and STM, and analyzed the observed morphology by comparison to molecular models. The PCBM bilayer revealed two distinct configurations on HOPG with different heights, and only one configuration on graphene. Post thermal annealing can induce merging of the bilayer nanostructures. Our results will shed light on improvement of the energy efficiency in solar cells containing graphene and organic molecules, by increasing the donor–acceptor interface area.

Acknowledgments

We would like to thank Professor Ted Einstein for helpful discussions. CC and CT acknowledge the financial support provided for this work by the US Army Research Office under the grant W911NF-15-1-0414. KP and JB was supported by US National Science Foundation DMR-1206354.

ORCID iDs

Chenggang Tao  <https://orcid.org/0000-0002-6609-0219>

References

- [1] Zhao W C, Li S S, Yao H F, Zhang S Q, Zhang Y, Yang B and Hou J H 2017 Molecular optimization enables over 13% efficiency in organic solar cells *J. Am. Chem. Soc.* **139** 7148–51
- [2] Cui Y, Yao H F, Gao B W, Qin Y P, Zhang S Q, Yang B, He C, Xu B W and Hou J H 2017 Fine-tuned photoactive and interconnection layers for achieving over 13% efficiency in a fullerene-free tandem organic solar cell *J. Am. Chem. Soc.* **139** 7302–9
- [3] Xiao Z, Jia X and Ding L M 2017 Ternary organic solar cells offer 14% power conversion efficiency *Sci. Bull.* **62** 1562–4
- [4] Hoppe H and Sariciftci N S 2004 Organic solar cells: an overview *J. Mater. Res.* **19** 1924–45

- [5] Sariciftci N S, Smilowitz L, Heeger A J and Wudl F 1992 Photoinduced electron-transfer from a conducting polymer to buckminsterfullerene *Science* **258** 1474–6
- [6] Bagher A M 2014 Introduction to organic solar cells *Sustain. Energy* **2** 85–90
- [7] Gunes S, Neugebauer H and Sariciftci N S 2007 Conjugated polymer-based organic solar cells *Chem. Rev.* **107** 1324–38
- [8] Scharber M C, Wuhlbacher D, Koppe M, Denk P, Waldauf C, Heeger A J and Brabec C L 2006 Design rules for donors in bulk-heterojunction solar cells—towards 10% energy-conversion efficiency *Adv. Mater.* **18** 789
- [9] Wienk M M, Kroon J M, Verhees W J H, Knol J, Hummelen J C, van Hal P A and Janssen R A J 2003 Efficient methano[70]fullerene/MDMO-PPV bulk heterojunction photovoltaic cells *Angew. Chem., Int. Ed.* **42** 3371–5
- [10] Liang Y Y, Xu Z, Xia J B, Tsai S T, Wu Y, Li G, Ray C and Yu L P 2010 For the bright future-bulk heterojunction polymer solar cells with power conversion efficiency of 7.4% *Adv. Mater.* **22** E135
- [11] Padinger F, Ritterger R S and Sariciftci N S 2003 Effects of postproduction treatment on plastic solar cells *Adv. Funct. Mater.* **13** 85–8
- [12] Muhlbacher D, Scharber M, Morana M, Zhu Z G, Waller D, Gaudiana R and Brabec C 2006 High photovoltaic performance of a low-bandgap polymer *Adv. Mater.* **18** 2931
- [13] Li G, Shrotriya V, Yao Y and Yang Y 2005 Investigation of annealing effects and film thickness dependence of polymer solar cells based on poly(3-hexylthiophene) *J. Appl. Phys.* **98** 043704
- [14] Ma W L, Yang C Y, Gong X, Lee K and Heeger A J 2005 Thermally stable, efficient polymer solar cells with nanoscale control of the interpenetrating network morphology *Adv. Funct. Mater.* **15** 1617–22
- [15] Wei G D, Wang S Y, Sun K, Thompson M E and Forrest S R 2011 Solvent-annealed crystalline squaraine: PC70BM (1:6) solar cells *Adv. Energy Mater.* **1** 184–7
- [16] Dang M T, Hirsch L and Wantz G 2011 P3HT:PCBM, best seller in polymer photovoltaic research *Adv. Mater.* **23** 3597–602
- [17] Bonaccorso F, Colombo L, Yu G H, Stoller M, Tozzini V, Ferrari A C, Ruoff R S and Pellegrini V 2015 Graphene, related two-dimensional crystals, and hybrid systems for energy conversion and storage *Science* **347** 1246501
- [18] Quesnel E et al 2015 Graphene-based technologies for energy applications, challenges and perspectives *2d. Mater.* **2** 030204
- [19] Zhang Y Y, Hu J P, Bernevig B A, Wang X R, Xie X C and Liu W M 2009 Localization and the Kosterlitz–Thouless transition in disordered graphene *Phys. Rev. Lett.* **102** 106401
- [20] Hong W J, Xu Y X, Lu G W, Li C and Shi G Q 2008 Transparent graphene/PEDOT-PSS composite films as counter electrodes of dye-sensitized solar cells *Electrochem. Commun.* **10** 1555–8
- [21] Lee Y Y, Tu K H, Yu C C, Li S S, Hwang J Y, Lin C C, Chen K H, Chen L C, Chen H L and Chen C W 2011 Top laminated graphene electrode in a semitransparent polymer solar cell by simultaneous thermal annealing/releasing method *ACS Nano* **5** 6564–70
- [22] Wang X, Zhi L J and Mullen K 2008 Transparent, conductive graphene electrodes for dye-sensitized solar cells *Nano Lett.* **8** 323–7
- [23] Wu J B, Becerril H A, Bao Z N, Liu Z F, Chen Y S and Peumans P 2008 Organic solar cells with solution-processed graphene transparent electrodes *Appl. Phys. Lett.* **92** 263302
- [24] Takeuchi O, Takeuchi N, Ochiai T, Kato H, Yoshida S and Shigekawa H 2014 Microscopic description of the current-voltage characteristics of a bulk-heterojunction organic solar cell under illumination *Appl. Phys. Express* **7** 021602
- [25] Chen D A, Nakahara A, Wei D G, Nordlund D and Russell T P 2011 P3HT/PCBM bulk heterojunction organic photovoltaics: correlating efficiency and morphology *Nano Lett.* **11** 561–7
- [26] Vanlaeke P et al 2006 P3HT/PCBM bulk heterojunction solar cells: relation between morphology and electro-optical characteristics *Sol. Energy Mater. Sol. Cells* **90** 2150–8
- [27] Peet J, Kim J Y, Coates N E, Ma W L, Moses D, Heeger A J and Bazan G C 2007 Efficiency enhancement in low-bandgap polymer solar cells by processing with alkane dithiols *Nat. Mater.* **6** 497–500
- [28] Otero R, Ecija D, Fernandez G, Gallego J M, Sanchez L, Martin N and Miranda R 2007 An organic donor/acceptor lateral superlattice at the nanoscale *Nano Lett.* **7** 2602–7
- [29] Masui A, Sakaue H, Takahagi T and Suzuki H 2016 Intermixing behaviors of PCBM with CuPc on Au(111) surface *Chem. Phys. Lett.* **661** 215–8
- [30] Gallego J M, Ecija D, Martin N, Otero R and Miranda R 2014 An STM study of molecular exchange processes in organic thin film growth *Chem. Commun.* **50** 9954–7
- [31] Shao Q, Tskipuri L and Reutt-Robey J E 2014 Vertical phase separation in bilayer [6,6]-phenyl-C-61-butyric acid methyl ester:zinc phthalocyanine films *J. Phys. Chem. C* **118** 18612–7
- [32] Zheng L D, Liu J G and Han Y C 2013 Polymer-regulated epitaxial crystallization of methanofullerene on mica *Phys. Chem. Chem. Phys.* **15** 1208–15
- [33] Hoppe H and Sariciftci N S 2006 Morphology of polymer/fullerene bulk heterojunction solar cells *J. Mater. Chem.* **16** 45–61
- [34] Jin Z W and Wang J Z 2014 PIN architecture for ultrasensitive organic thin film photoconductors *Sci. Rep.* **4** 5331
- [35] Pratihari P, Ghosh S, Stepanenko V, Patwardhan S, Grozema F C, Siebbeles L D A and Wurthner F 2010 Self-assembly and semiconductivity of an oligothiophene supergelator *Beilstein J. Org. Chem.* **6** 1070–8
- [36] Ji A C, Xie X C and Liu W M 2007 Quantum magnetic dynamics of polarized light in arrays of microcavities *Phys. Rev. Lett.* **99** 183602
- [37] Yang X N, van Duren J K J, Rispen M T, Hummelen J C, Janssen R A J, Michels M A J and Loos J 2004 Crystalline organization of a methanofullerene as used for plastic solar-cell applications *Adv. Mater.* **16** 802
- [38] Tskipuri L, Shao Q and Reutt-Robey J 2012 Molecular ordering in PCBM-Au(111) interface formation *J. Phys. Chem. C* **116** 21874–9
- [39] Ecija D, Otero R, Sanchez L, Gallego J M, Wang Y, Alcamí M, Martín F, Martín N and Miranda R 2007 Crossover site-selectivity in the adsorption of the fullerene derivative PCBM on Au(111) *Angew. Chem., Int. Ed.* **46** 7874–7
- [40] Li H, Duan Y Q, Coropceanu V and Bredas J L 2009 Electronic structure of the pentacene-gold interface: a density-functional theory study *Org. Electron.* **10** 1571–8
- [41] Huebener K, Scheloske M, Hauschild J, Harneit W, Zehl G and Fiechter S 2006 AFM investigation of the formation of one-dimensional structures of C₆₀ shuttles on HOPG *Phys. Status Solidi b* **243** 2990–4
- [42] Walczyk W, Schon P M and Schonherr H 2013 The effect of PeakForce tapping mode AFM imaging on the apparent shape of surface nanobubbles *J. Phys.: Condens. Mater* **25** 184005
- [43] Girard C, Lambin P, Dereux A and Lucas A A 1994 Van-der-Waals attraction between two C₆₀ fullerene molecules and physical adsorption of C₆₀ on graphite and other substrates *Phys. Rev. B* **49** 11425–32

- [44] Wang Y, Alcami M and Martin F 2008 Understanding the supramolecular self-assembly of the fullerene derivative PCBM on gold surfaces *Chemphyschem* **9** 1030–5
- [45] Girifalco L A, Hodak M and Lee R S 2000 Carbon nanotubes, buckyballs, ropes, and a universal graphitic potential *Phys. Rev. B* **62** 13104–10
- [46] Branz W, Malinowski N, Enders A and Martin T P 2002 Structural transition in $(C_{60})_n$ clusters *Phys. Rev. B* **66** 094107
- [47] Wang C I and Hua C C 2015 Solubility of C_{60} and PCBM in organic solvents *J. Phys. Chem. B* **119** 14496–504
- [48] Gravié P A, Devel M, Lambin P, Bouju X, Girard C and Lucas A A 1996 Adsorption of C_{60} molecules *Phys. Rev. B* **53** 1622–9
- [49] Igathinathane C, Pordesimo L O, Columbus E P, Batchelor W D and Methuku S R 2008 Shape identification and particles size distribution from basic shape parameters using ImageJ *Comput. Electron. Agric.* **63** 168–82
- [50] Scott D W 1979 On optimal and data-based histograms *Biometrika* **66** 605–10